Mechanical performances of Hip implant design and fabrication with PEEK composite

Bankole I. Oladapo[a,*], S. Abolfazl Zahedi[a], Sikiru O. Ismail[b]

[a]School of Engineering and Sustainable Development, De Montfort University, LE1 9BH, Leicester, UK

[b]School of Physics, Engineering and Computer Science, University of Hertfordshire, AL10 9AB, England, UK

*Corresponding author's e-mail: bankolyable01@gmail.com

Abstract

Artificial bone implant materials need porosity for nutrient distribution, moderate pore size to provide cell cultures and bone-like mechanical properties. The homogenisation of discrepancies between the microstructure of implants and bone is an important subject. This research aims to design microstructures with poly ether-ether-ketone (PEEK) and its composites to improve the compatibility of implants. Porous hip bone implants fabricated by fused deposition modelling (FDM) are proposed to mimic natural bone with various homogenisation lattice structures and excellent properties. Five isotropic lattice structures with homogenisation control strategies are printed with PEEK and composite PEEK with reduced graphene oxide (rGO) and calcium hydroxyapatite (cHAp). An examination is performed on a three-dimensional (3D) distribution of the effective module surface of the five composite porous unit lattice structures. The relationship between the modulus of elasticity, anisotropy and cell parameters are thoroughly investigated by finite element analysis (FEA). Analysis of the surface treatment used to create micropores in the scaffolding and the nanostructure yields a bioactive PEEK/hydroxyapatite (HAp) composite with various control configuration distributions and cell growths. The functionalised biocompatibility and degradability of rGO/HAp composite in various ratios to PEEK, and their nanostructure arrays, are studied by a surface functionalisation approach. The improved design eliminates slight imperfections, allowing for a more stable structure. The controlled homogenisation, porosity and particle size distribution helps to increase cellular infiltration and biological integration of the PEEK and hip implant composites.

Keywords: Hip implant; Homogenisation; PEEK/rGo/cHAp, Lattice structures; Biocompatibility

1. Introduction

Additive manufacturing (AM) was initially developed as a resource for the rapid prototyping of industrial products. Nowadays, this technique is used in several domains of knowledge, including the medical sector [1-3]. AM is used extensively in the health sector to aid diagnosis, support complicated surgery, and customise customised artificial implants [4-6]. A set of two-dimensional (2D) images in the international standard format [6,7], relative to the sliced planes of the body, is used to reconstruct three-dimensional (3D) volumes of anatomical regions. A simple 3D virtual model can be transformed into a standard pattern to be interpreted by AM equipment. Layer-by-layer natural reproduction provides excellent and quick results for forms that would be difficult or even impossible to produce with established industrial technologies [8-10]. The technique of manufacturing by layers and the production of free forms are used with 3D printing.

All AM techniques have the following processing steps: (i) 3D modelling of the part; (ii) generation of 3D geometry in standard tessellation language (STL), a standard file format for AM that creates an approximation of the surface using a mesh; (iii) checking the integrity of the data file; (iv) manufacturing by layer; and (v) post-processing of the part when necessary. Two standard machines for AM of medical equipment are selective laser

sintering (SLS) and fused deposition modelling (FDM). In SLS, carbon dioxide (CO_2) lasers burn powdered materials [11-13]. The machine burns parts by using a laser beam on powder, according to the 2D geometry of the workpiece. This process is repeated for each thin layer until the product is complete. In FDM, the part is produced in the same way as SLS, but the input material is filament [14-16].

AM can print specific types of material, which, for health-related applications, should be biocompatible. Poly ether-ether-ketone (PEEK) is one such biocompatible material, but its high melting temperature AM by PEEK printing is not easy. Bone implant with a PEEK structure enhances implant quality in several respects, including fracture and fatigue strength. FDM technology allows the manufacture of biometric PEEK scaffolds, with a recent prototyping technique being the electron beam machine (EBM). According to the part's design, the powder is cast by an electron beam, and this rapid PEEK prototyping technology makes it possible to control the large pore geometries and functional graded pore distribution (FGPD) [17-20]. Technologies using high energy beams allow for the construction of ceramic parts, and may soon lead to the fabrication of pure calcium hydroxyapatite scaffolds with upper dimensional and geometric control of the pores and spatial control of the volume of the implant. There is a release of vapour when samples are subjected to high power lasers, but this can be solved by a trial-and-error method by reduction of the temperature of the layer of dust on the construction platform. Removal of the roll speed, an increase in the coating thickness, or double scanning with the laser in up to 10 layers (~2.5 mm), with 1 mm holes.

AM has several applications in the health sector and is now employed in many hospitals. The most prominent are: (1) polymer or plaster models for planning and surgical training; (2) polymer guides for bone-piercing and cutting; and (3) the modelling of implants [21-23]. Other applications are used globally in research, such as: (i) scaffolds of biocompatible PEEK, polymer or composite; (ii) implants constructed of PEEK, composite, polymer or ceramic; and (iii) bio-impressions of organs. Health applications of AM can be divided, from a bioengineering perspective, into two branches, indirect and direct. The complicated processes used can require melds for the final construction of the implants, but ideally, implants should be made without subsequent processing. Drill aid guides or osteotomies can be produced directly in the AM process. Direct methods for ceramics and PEEK have recently been launched in the market, with the latter tested for customised implants, including femoral and mandible implants. Surgical planning techniques using AM have evolved for at least 15 years, mainly in the field of craniofacial reconstruction. However, AM has not evolved sufficiently for applications with significant loading requirements [24-26].

AM methods represent a significant advance in printing complex 3D geometries for bone architecture and an essential step towards the geometric optimisation of 3D configurations. In AM, appropriate dimensional accuracy can be achieved for medical products, and these can be customised for patients. In the subsequent processes, the polymer-rich phase becomes a matrix and the polymer-lean stage turns into pores when the solvent is evaporated. This revolutionary method is critical to cell and medical device industry applications. This research applies to biomedical cell devices, where miniaturised scaffolds are required. This paper deals with the production of lattices for hip implants and porosity analysis. A bioactive PEEK composite with an additional control configuration distribution is used for the fabrication of implants. With a surface functionalisation approach, the functionality of the biocompatibility and degradability of PEEK composite is enhanced. Non-biological cell microdevices also benefit from this work on bone-implant applications due to the low weight and high capacity method used.

2. Materials and method

In this research, FDM technology is applied to print scaffolds. The properties of the PEEK used are presented in Table 1. The compression surfaces of the lattices are polished to be parallel up to a maximum of 10 μm. The extrusion temperature is set at 380–410°C, and the printing speed is 40 mm/sec. The bead width of each print line is 0.4 mm, and the layer thickness of the PEEK filler is 0.2 mm.

**Table 1** Material properties of the PEEK filament.

Description	Value PEEK	Test method
Melting temperature	345 – 400 °C	---
Glass-transition temperature	143 °C	---
Density	1.36 g/cm^3	ISO 1183
Young's modulus	3.850 GPa	ISO 527
Tensile strength	100 MPa	ISO 527
Impact strength notched Izod	---	ISO 180/A

The first task is constructing custom implants with the human femur's high mechanical strength as an alternative to standard implants [27-29]. These implants are made directly in PEEK using AM equipment from a virtual model generated in Mountain 8 Premium package. As described in [30-32], the equipment uses PEEK biomaterials in filament and powder form as raw material. According to the manufacturer, as well as providing physical bio-models directly in biomaterial with high fidelity to virtual bio-models, the equipment can construct scaffolds with varied geometries, dimensions, and spatial distributions. Fig.1 shows the five hip implant unit strut applications studied in this research. It is worth mentioning that the unit cells are homogenised later, and the final production of the hip implant is based on an isotropic lattice. The lattice structures are designed in Creo software, modified, and simulated to find homogenisation in the nTopology package, and ANSYS Workbench is used for finite element analysis (FEA).
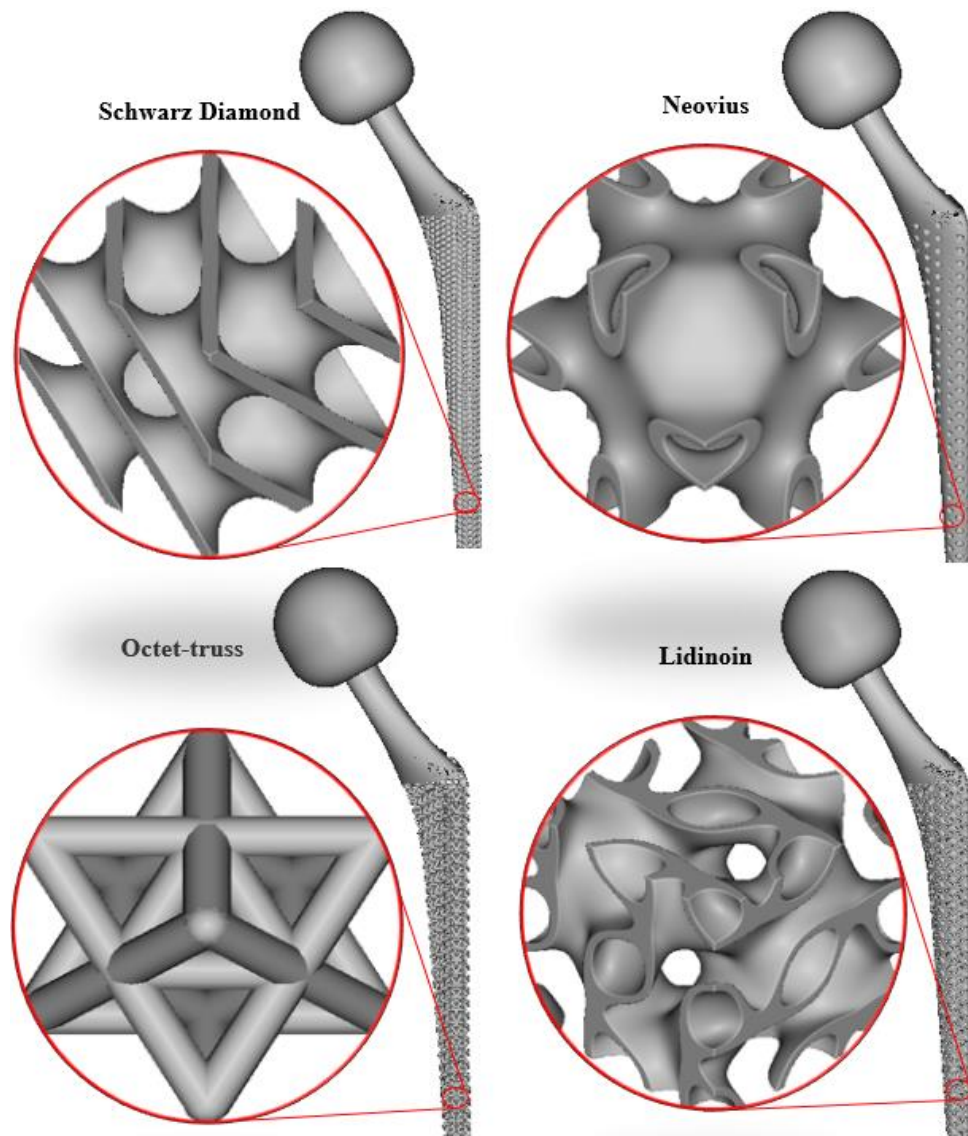
Fig. 1. Lattice cells in hip implant struts

Fig. 2 shows the schematic of the experimental study. The diagram illustrates the extrusion printing system, mechanical testing process and implantation. The techniques outlined in this work for the direct production of PEEK parts for immediate implant manufacturing could constitute a revolution in medicine since they innovatively create the possibility of the quick production of implants with high micro and macro dimensional compliance [33-35].
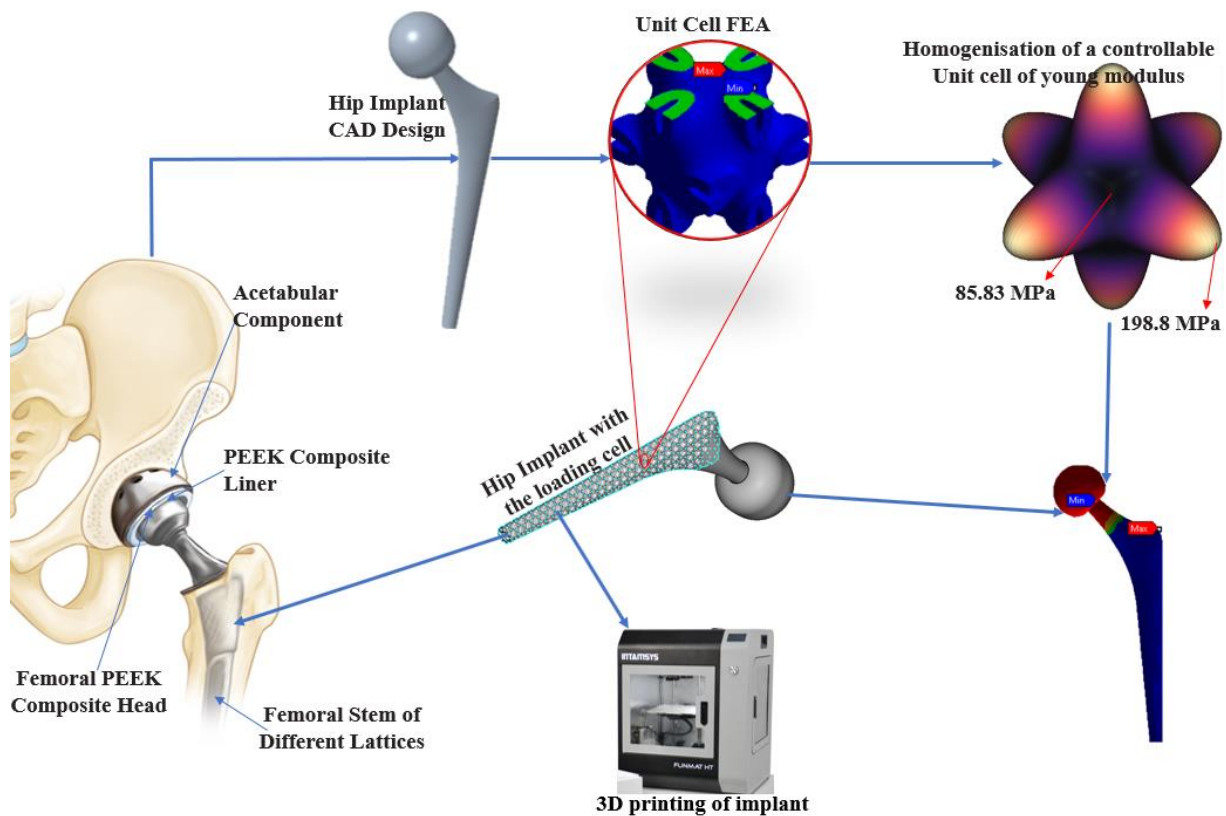
Fig. 2. Schematic of the experimental process of fabricating hip implants with composite PEEK

3. Material properties

Pure graphene monolayers are reported to have mechanical properties with Young's modulus of 1000 GPa, and internal tensile strength of 130.5 GPa. An essential factor in the quality of graphene oxide is the pH when a dispersion of graphene oxide solution is produced by the hummer method, usually between 2 and 3 if the washing steps are not included in the manufacturing process. The acidic nature (pH = 2-3) of unwashed graphene oxide significantly worsens its properties, hence graphene oxide products require repeated rinsing with large amounts of distilled water. Our graphene oxide dispersion is almost neutral, with a pH of approximately 6-7, obtained by washing and drying, dissolving water, distillation and sonication. Single-layer reduced graphene oxide (rGO), a new graphene-based nanomaterial, has a wide range of applications because of its atomic thickness and other excellent properties. It has good solubility in chemical or thermal water and organic solvents, facilitating the production of rGO solution using the wet chemical method. It is inexpensive and plentiful, and rGO products are resistant and ready to use. In a refurbished hummer, water, methanol, DMF, NMP, etc. is used to prepare a single-layer rGO surfactant-free dispersion suitable for a wide variety of environments, such as ultrasound [36-37]. The structure is placed in an oven which is slowly heated to 320 ºC in a vacuum chamber. This is just below the 350 ºC melting point but hot enough to vaporise the structure's organic materials and leave the PEEK behind. This

heating method is known as pyrolysis because the process evaporates a significant amount of the structure's material, meaning its dimensions contract by 80%, but it retains its shape and proportions.

4. SEM and mechanical test

The Hitachi S416 scanning electron microscope (SEM) is used to observe the dispersion and adhesion properties between the nano rGO flakes and the cracked mortar surfaces. After analysing the samples, they are incubated for 28 days. The fractured body is cut into approximately 10×5×4 mm samples. They are covered with a 3 nm platinum/palladium layer to improve conductivity. The composition of the cement matrix is determined in two ways: X-ray distributed energy analysis is used to determine the material's constituent components, and X-ray diffraction (XRD) is used to determine its crystalline phase. Quantitative analysis of the crystalline and amorphous nanocomposite hydrate cement steps is performed using the internal standard XRD technique. Crystal distances are determined using a Bruker X-ray diffusion meter. The AXS D8 Advance X-ray (XRD) is used with CuKα radiation (λ = 1,540 Å), a scanning speed of 0.02 °/s in the range 2θ 4-70°, an acceleration of 40 kV, and an acceleration voltage of 30 mA. Episodes are defined using database-based matching software. The ASTM C307-03 standard test is used to determine the tensile strength of the cement with various rGO percentages compared to control samples without rGO after curing. The depth and width at the waist of each model is measured within ±0.5 mm. The model is loaded into a tensile testing machine with a crosshead speed of 5 to 6.4 mm/min.

5. *In vitro* test

The cells are cultivated in 10% foetal bovine serum in a Dulbecco Modified Eagle Medium (DMEM) culture media pouch. This a medium for the development of various mammalian cells. The updated DMEM has a fourfold increase in amino acids and vitamins from the original Eagle medium. The cells are cultivated in CO_2 at 37 °C and 5% humidity. The culture medium is substituted regularly. The formulation used is 9.9 g of powder to 1 litre of DMEM, supplemented with 3.7 g of sodium bicarbonate for every 1 litre. One bag of powder (15.25 g) is poured into a container, then deionised water is added to make the mix up to 450 ml, and the mixture is stirred with a magnetic stirrer bar. A further 0.5 litres of deionised water is added and the content is heated to encourage the powder to dissolve in the water, and it is then autoclaved at 121°C for 15 or 20 minutes. 125 ml of 3-chemical nutrient agar solution forms the culture medium. It contains everything necessary for most experiments with no need to add other ingredients or biological fluid for cell culture. It is prepared in a microwave bottle, in about 60 seconds, or a hot water bath.

6. Results and discussion

The SEM analysis of PEEK/HAp is shown in Fig. 3. It shows a range of nanoparticle thresholds ranging from -60.89 to 39.12 nm, with a Daubechies waviness high-pass filter image and robust Gaussian filter at 285 nanoparticles. The particle analysis settings are shown in Fig. 3(b). A watershed detection method is used with 1336 nanoparticles, having a mean projected area of 37.48 µm², an equivalent diameter of 5.837 µm, height of 14.36 nm and roundness, compatibility and pitch of 0.5803, 0.7573 and 7.323 µm, respectively. The scaled sample profile analysis in the 0.8 mm Gaussian filter and the roughness of the Daubechies wavelet filter show slice luminance conversion of the nanoparticles and the frequency luminance spectrum conversion micro-nano

particles. This shows the osseointegration and biomechanical properties of the PEEK/HAp scaffolds used in tissue engineering.
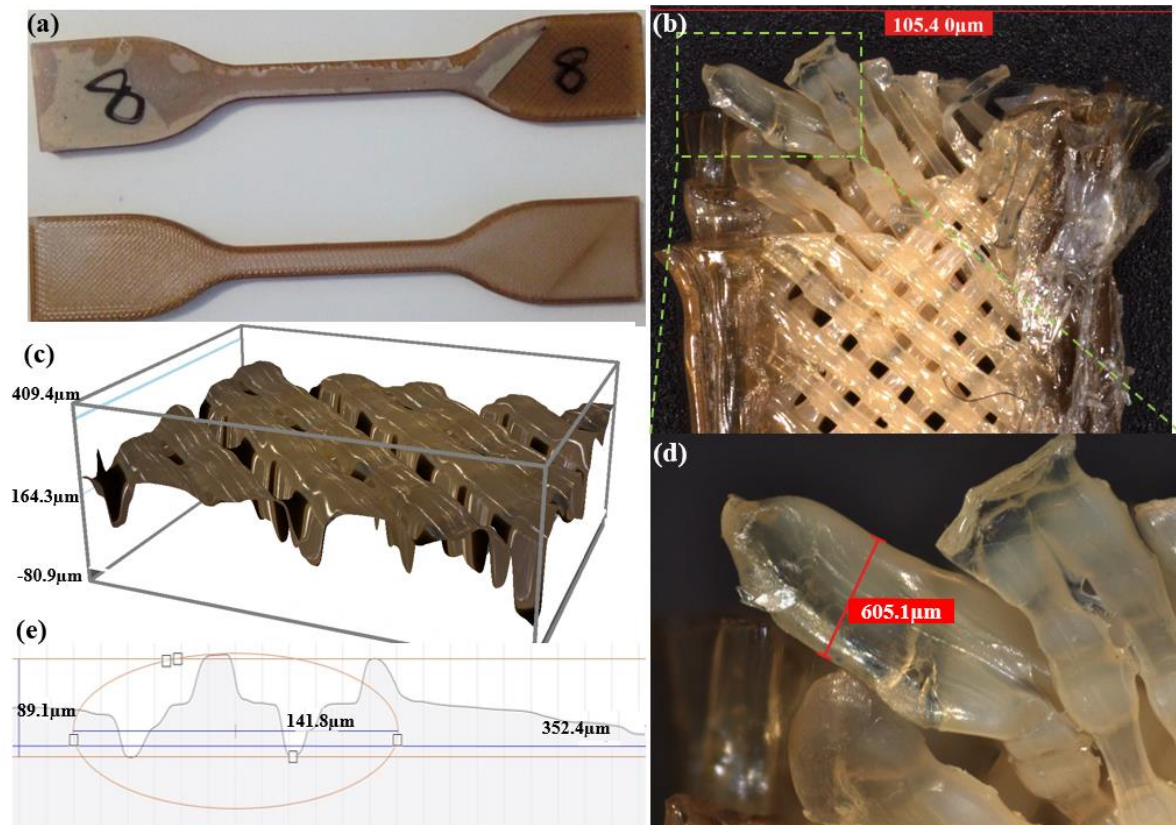
Fig. 3. (a) 3D-printed tensile reference sample of PEEK, (b) a sample with porosity 105 µm after tensile fracture, (c) microscopic profile of the 3D model, (d) 500× magnification of a 605 µm fibre, (e) profile graph of the 3D sample with pixels of 1.2872 ms and a resolution of 0.2225 µm/pixel

6.1. Lattices of 3D nanostructure

Composite materials are basic materials used in creating ultrafine 3D structures for bone implants built using AM. 3D printing can produce porous PEEK with greater capacity and lower weight. Studies have established a new 3D-printed bone method using a controlled porosity micro-reticular structure. Designs in PEEK composite with porous architectures can lead to higher inflow capacities of body fluid. Such structures allow cells to penetrate the volume of the bone structure, leading to very high utilisation and greater cell storage capacity. In a typical design, 10-30% of the total composite volume is not used. 3D printing creates a porous microgrid architecture, which enables efficient cell and fluid body transport across the entire bone structure and increases bone charge rates [38-40]. The lattice architecture achieved with 3D printing provides channels for the effective transport of cells and fluid within the material. Fig 4. shows the computer-aided design (CAD) of various lattices for hip implant applications in 3D and 2D views and the homogenisation of each lattice.
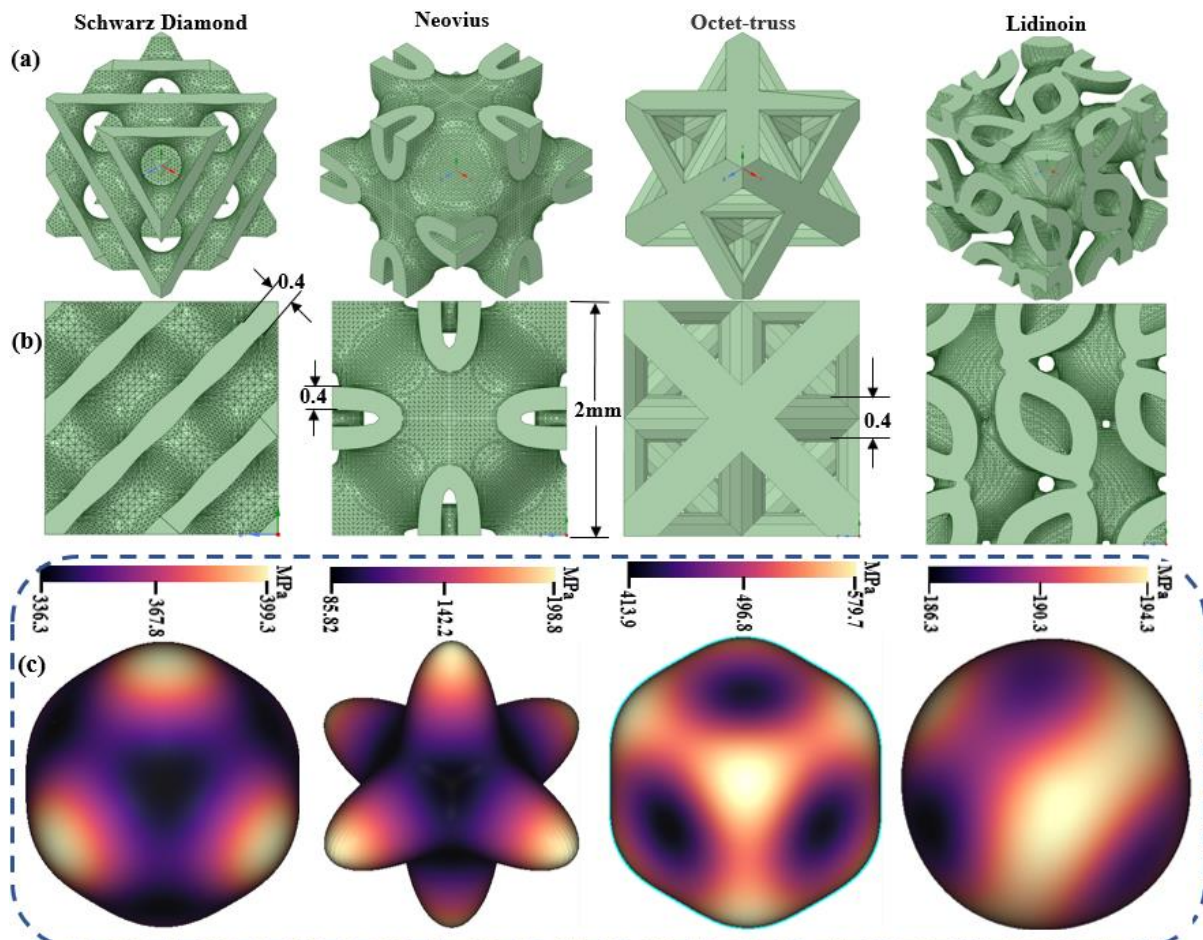
Fig. 4. CAD of hip implant lattices: (a) 3D view, (b) 2D view with dimensions, and (c) homogenisation of each lattice

6.2. Mechanical behaviours

Fig. 5 shows a digital image of the generated scheme. Under the SEM, excellent characteristics are seen for diamond shapes, cell walls and clearly defined pores. The surface roughness is compared to traditional EBM methods [33] and shown to be better than the high entropy generated by EBM [41]. The wall thickness and pore size are designed with less than 10% difference. The pore size is about 10% smaller than projected, which is a desirable factor. Porosity is significantly associated, with a difference of less than 4%.
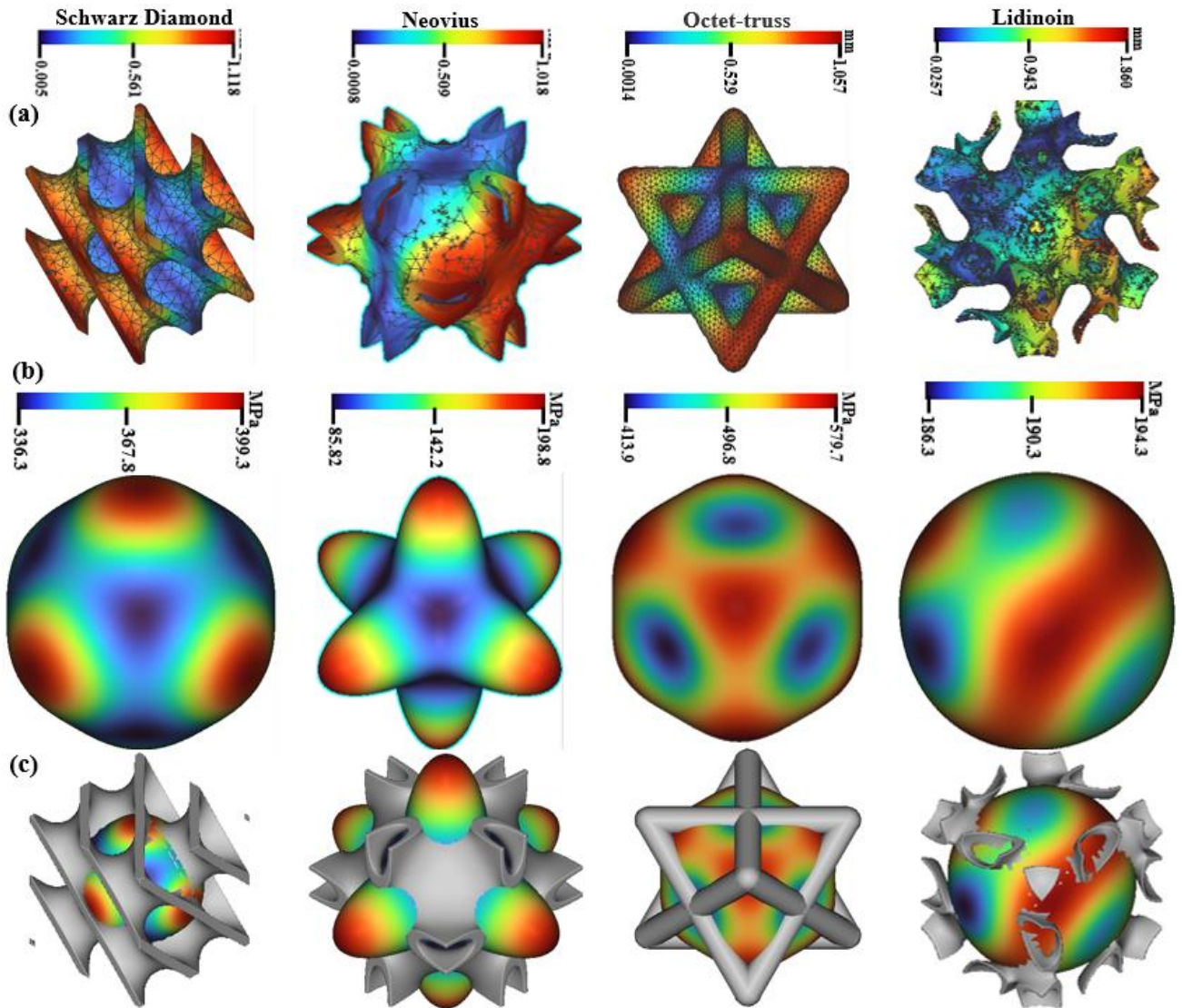
Fig. 5. (a) Displacement directional stress of a unit cell, (b) homogenisation of directional Young's modulus (MPa), and (c) behaviour of homogenisation within a unit cell

All models are in the range 46-60% porosity. Microstructure SEM plates constructed with cages are included in the material. An extremely thin layered mesh of ~0.25 μm is typical of the high strength PEEK produced by EBM, which is extensively covered in our previous study [33, 42, 43]. The microstructures of the base alloy are homogeneous throughout the complex architecture. The mechanical behaviours, including stress-strain curves and other results, representing compression stress of 0.3, are shown in Figs. 6-9.
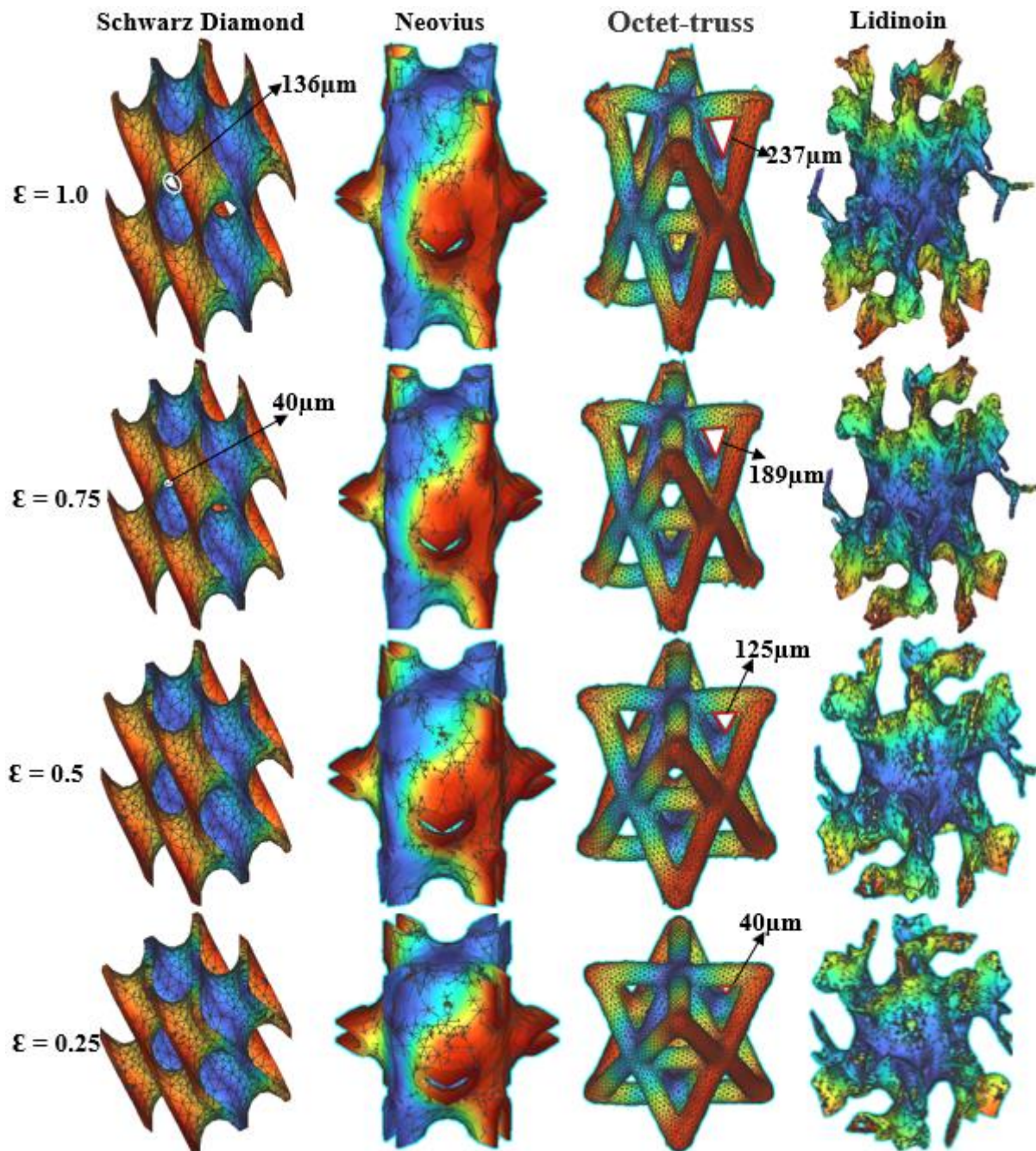
Fig. 6. Comparison between the FEA of the homogenisation of lattice CAD models, strain displacement (mm) behaviours of the models in z-direction after applying load

Based on the shape of the stress curves, all pressures generally follow the same trend as the plateau stresses of the network. After the elastic zone, the mesh provides resistance to compression, then collapses at post-maximal values, with similar relative densities. This shows that the Young's modulus and compressive strength are approximately 60% and 50% greater in PEEK/rGO/HAp with ratios of PEEK-69, cHAp-30, rGO-1 (wt%), in comparison to PEEK-78, cHAp-20, rGO-2 and PEEK-87, cHAp-10, rGO-3. The wall material is strongest in its natural resistance to compression. Interestingly, the lattice makes no implicit difference, and the hexagonal cut pores in the diamond have little effect on the hardness or strength.

Fig. 7 shows the mechanical testing of PEEK and its composites at various ratios of cHAp, ranging from 5 to 30 wt% with corresponding PEEK of 95 to 70 wt%, at intervals of 5 wt%.
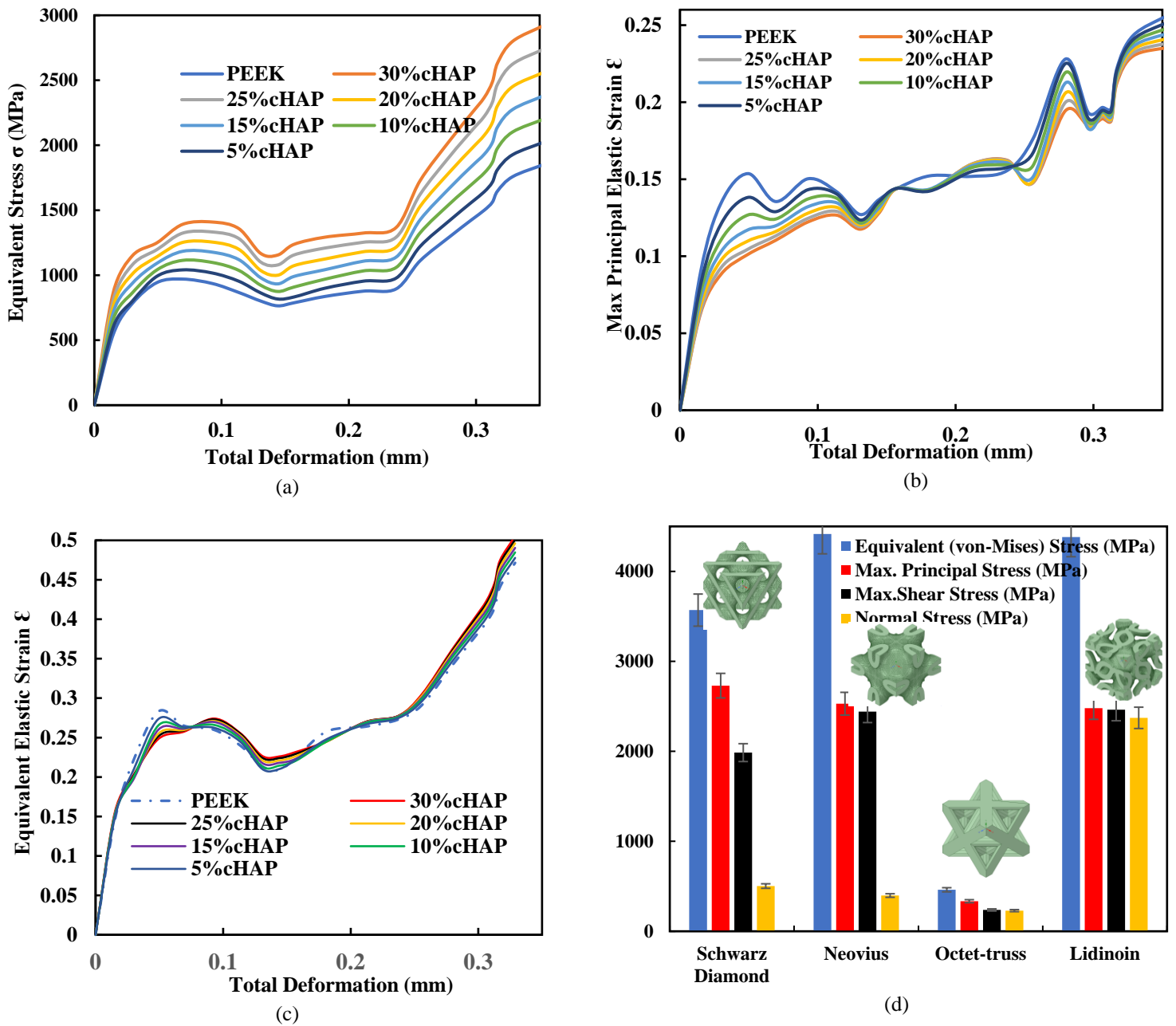
Fig. 7. (a) Compressive stress-deformation of PEEK/cHAp composites, (b) maximum principal elastic strain of PEEK/cHAp versus deformation, (c) analysis of equivalent elastic strain versus deformation, and (d) further stress analysis of each unit cell by microstructure

3D structures in various materials, from ceramic to organic compounds, are dchallengingto print if the designs are less than 50 microns in height or about half a human hair's width. Nanoscale 3D printing is done with a high-precision laser which excites a liquid at a specific location with just two photons or light particles. This provides ample energy to solidify liquid polymers but not enough to fuse PEEK, which does not respond to light in the

same way as the polymeric resins used to make nanoscale structures. As light interacts with a polymer, it hardens to form a specific structure.
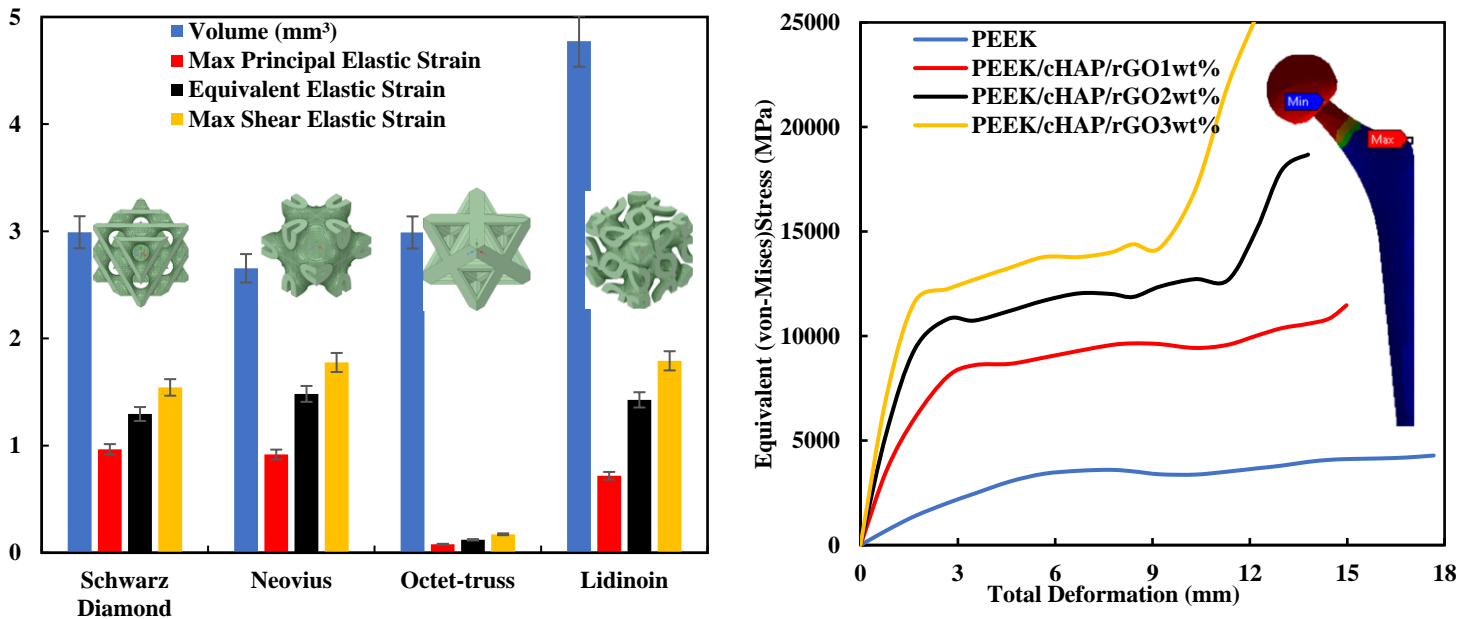

Fig. 8. Strength of the various lattice structures and von Mises stress analysis of the total deformation

Fig. 8(a) shows the strain for five different lattice structures and fig. 8(b) shows the von Mises stresses for three volume ratios of PEEK composite: sample 1, 69% PEEK, 30% cHAp, 1% rGO; sample 2, 78% PEEK, 20% cHAp, 2% rGO; and sample 3, 87% PEEK, 10% cHAp and 3% rGO. A chemical reaction is fundamentally impossible in PEEK: a solution containing organic bonds and molecules that adhere to materials to create a resin containing polymer carrying printable PEEK. Such as the scaffolding in the experiment described in which organic molecules create a liquid that closely resembles a bone implant. A structure is designed using computer software and built by 'zapping' the liquid with a two-photon laser. The laser creates chemical bonds between the organic molecules, hardening them to structural blocks.
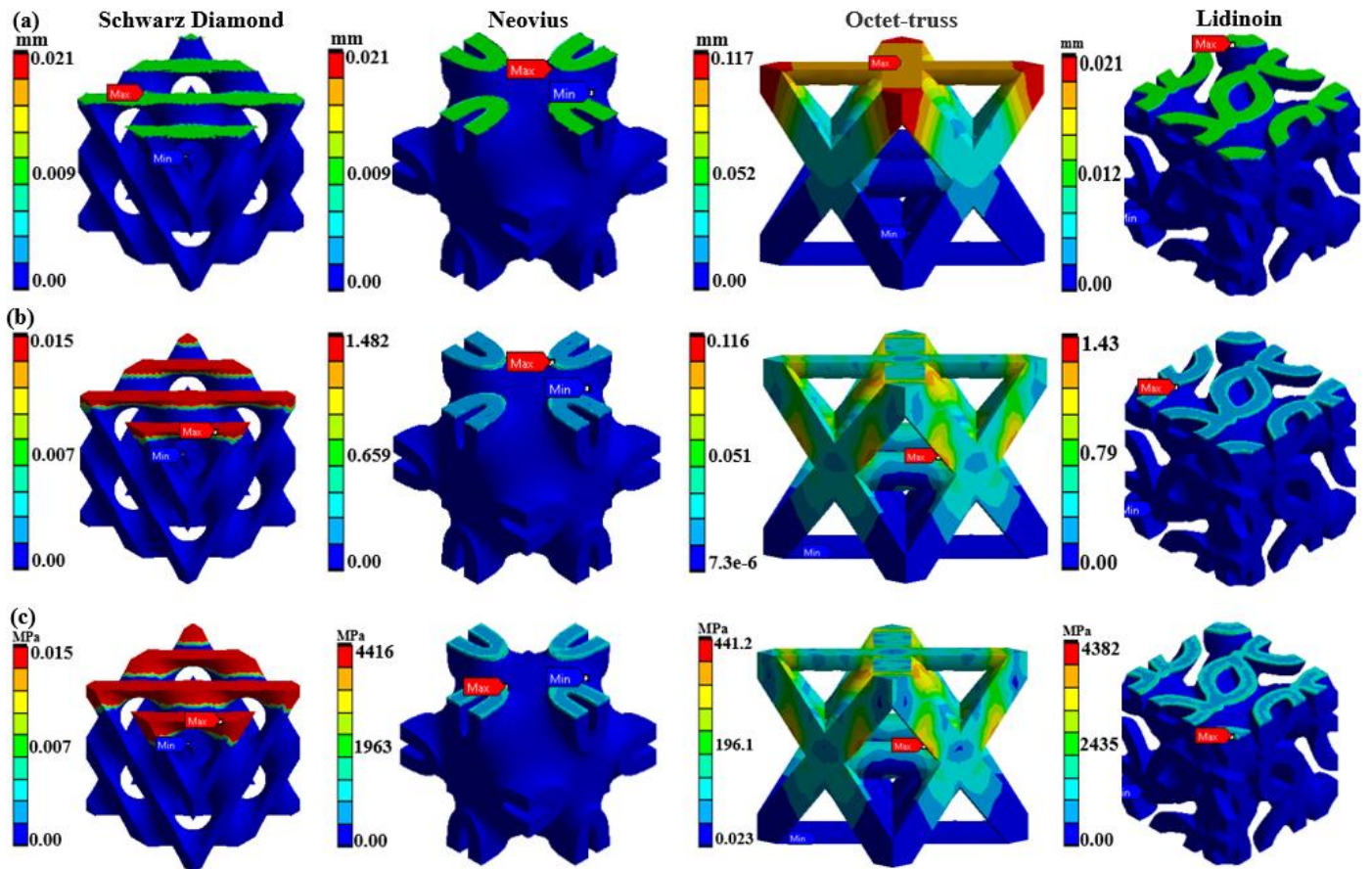
Fig. 9. Lattice structures of composites, with red representing the highest stress area after applying load: (a) total displacement of each unit cell, (b) unit cell equivalent elastic strain (mm/mm), and (c) unit cell equivalent (von Mises) stress (MPa)

Fig. 10 shows the FEA of PEEK/rGO/HAp hip implant composites with various ratios of constituents: PEEK-69, cHAp-30, rGO-1 (wt%), PEEK-78, cHAp-20, rGO-2, and PEEK-87, cHAp-10, rGO-3, with specific loading conditions. The FEA settings have a load step with explicit time integration, having an end time of 0.00001, in which the initial minimum and maximum time steps are program-controlled. The general time step safety factor is set to 0.9 as a minimum, and there are characteristic dimension diagonals with no automatic mass scaling. The beam time step safety factor is set to 0.5, with hexagonal integration of the shell sublayer during printing. The shell shear correction factor is set to 0.833, and the nodal shell thickness has average nodal pressure test integration. The program-control uses Euler domain controls for domain size definition, an accurate display, a perfect scope for all cells' body, and domain resolution definition. A geometry scoping method is used to calculate the time history and global coordinate system, as the program runs homogenisation and FEA results. The integration point results have an average display option with no average across bodies to estimate all stress, strain and safety factors. As seen in Fig. 10, the element of security favours PEEK-87, cHAp-10, rGO-3 (wt%), as it can withstand the stress of 25.32 GPa at the node of the hip implant with slight deformation of 9.29 mm, compared to PEEK with stress of 4.28 GPa and deformation of 17.70 mm.
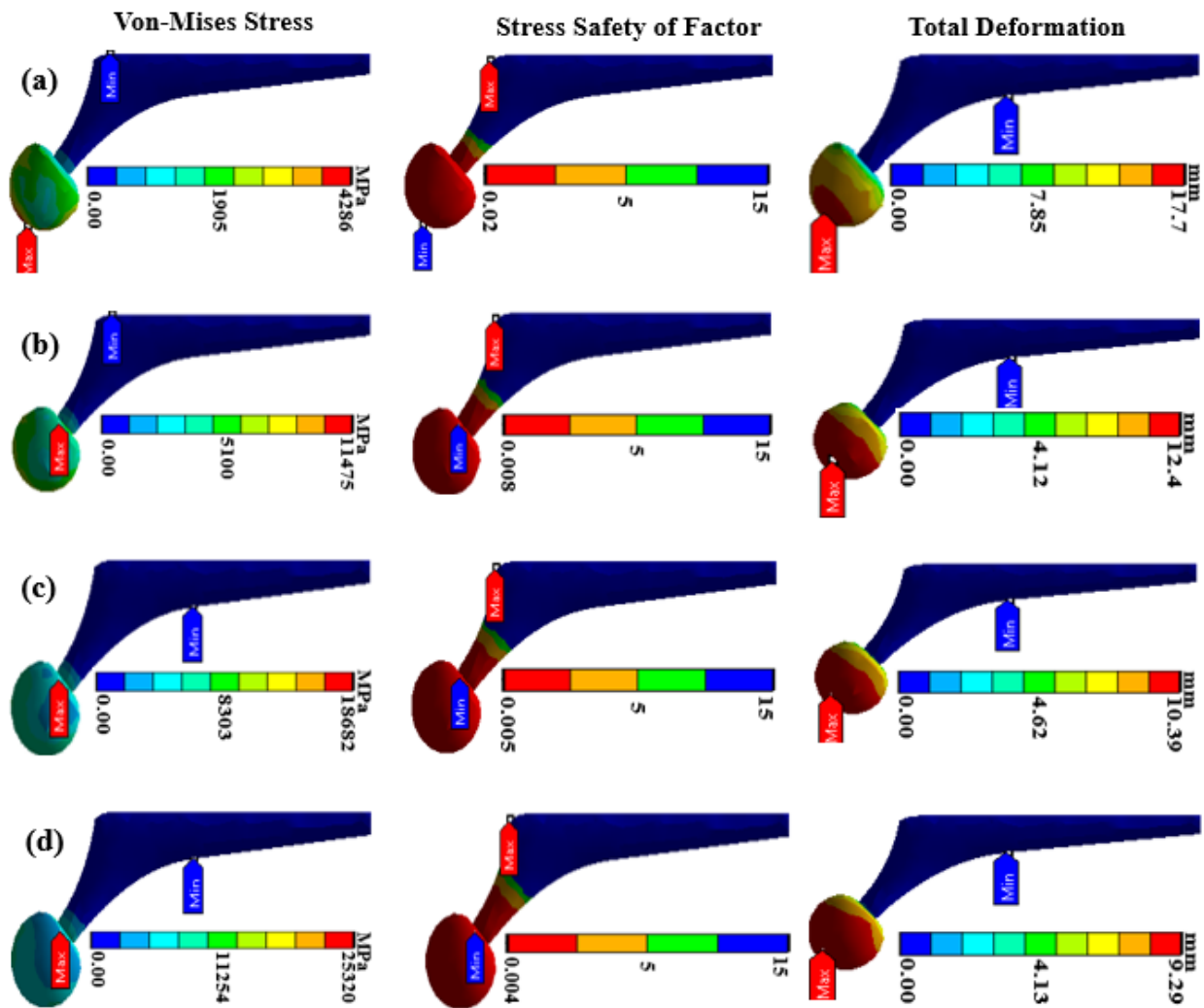
Fig. 10. FEA results for hip implant of PEEK and composite: (a) PEEK, (b) PEEK-69, cHAp-30, rGO-1, (c) PEEK-78, cHAp-20, rGO-2, and (d) PEEK-87, cHAp-10, rGO-3 (wt%).

6.3. In vitro cytotoxicity analysis

As shown in Fig. 11 and 12, an accumulation of cells is observed in the surface grooves, resulting from the deposition pattern of the manufacturing process. The PEEK/HAp composite cells are mixed in clusters, but the PEEK cells are dispersed. More prominent actin filaments are seen in PEEK/rGO/cHAp, which bind with adjacent cells. On day 14, there is a significantly higher relative behaviour of the PEEK/HAp alkaline cell phosphatase compound than PEEK p=0.005.5A-F. Similarly, more prominent actin filaments are seen in PEEK/HAp which is bound to adjacent cells. The PEEK/HAp is also thicker on the PEEK surface than in the cell nuclei. Fig. 13 shows the live/dead staining of cells attached to the FDM 3D-printed PEEK composite sample surfaces. After culturing the samples with the nutrient agar solution, this is observed at 50 µm of PEEK and PEEK/rGO/cHAp for a day. Significantly, 10 µm of PEEK/rGO/cHAp shows live-cell growth, which is increased at 20 µm. At 50 µm of PEEK, cells spread with tiny dead cells at the 7th day and more at the 14th day, while PEEK/rGO/cHAp cells grow circling small dead cells at the 7th and 14th days. Fig 12.
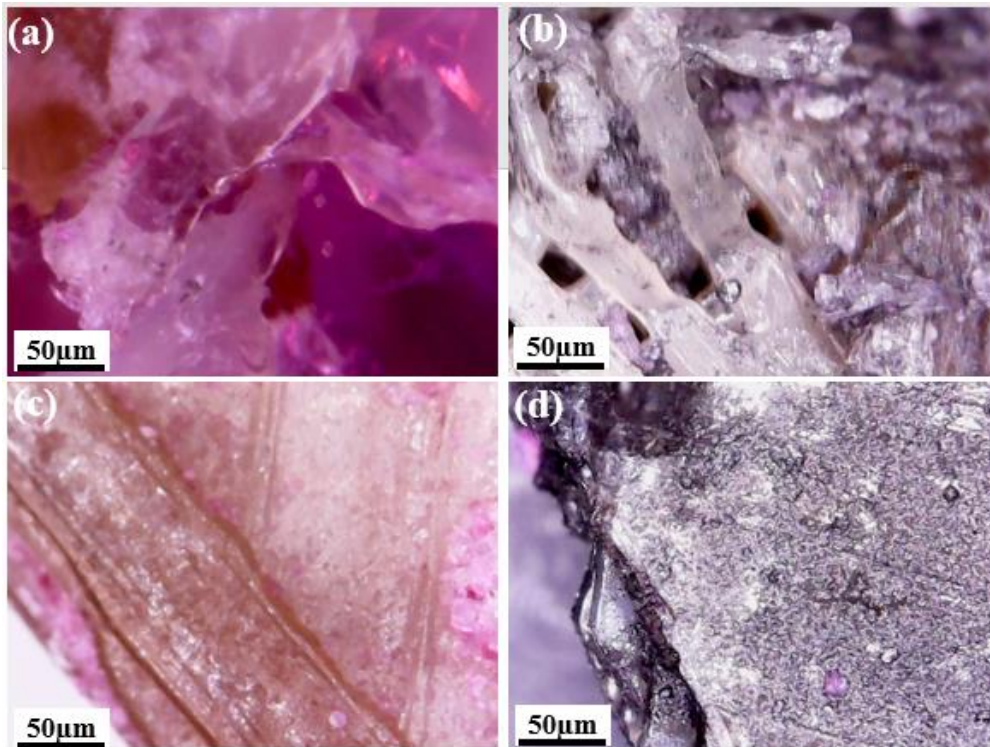
Fig. 11. Cells attached to sample scaffold surfaces using DMEM culture medium over days: (a) 50 µm of PEEK after 24 hours, (b) 50 µm of PEEK/rGO/cHAp composite scaffold after 24 hours, (c) 50 µm of PEEK after three days, (d) corresponding magnification of 50 µm of cell deposition of PEEK/rGO/cHAp.
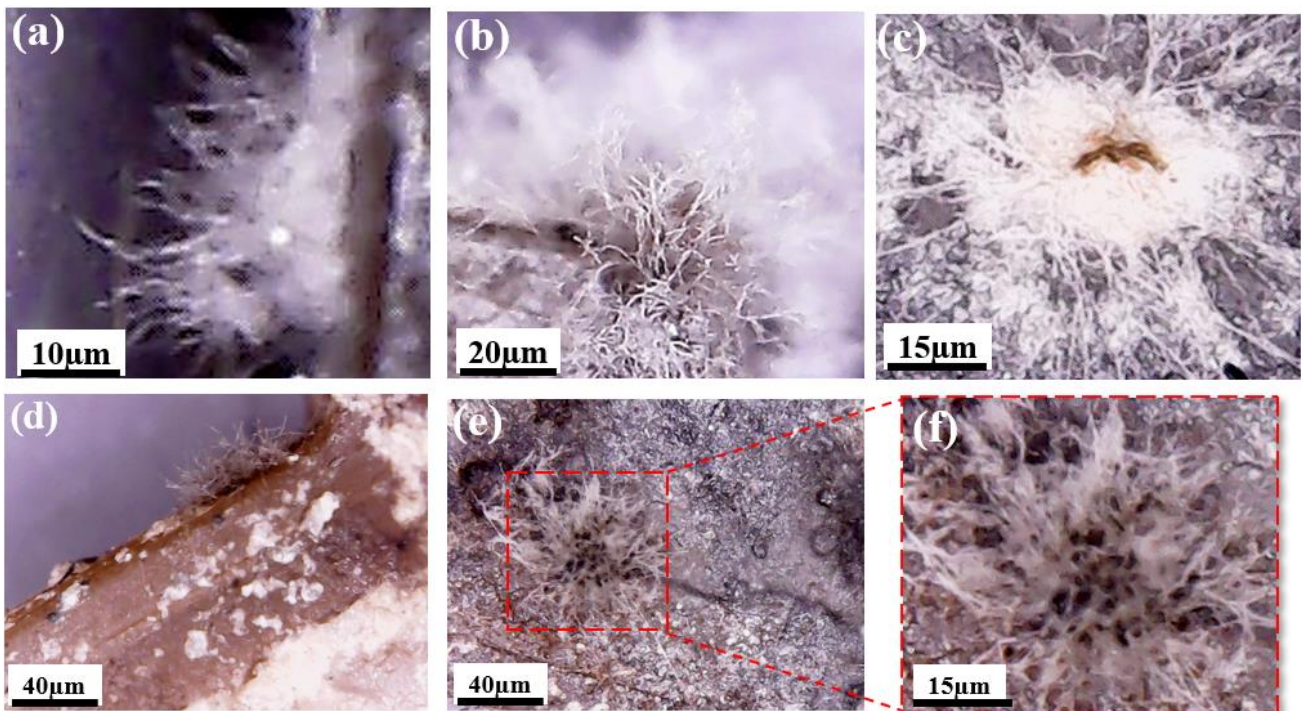

Fig. 12. Live/dead staining of cells attached to FDM 3D-printed PEEK composite sample surfaces after culturing with nutrient agar solution: (a) 10 µm of PEEK/rGO/cHAp showing live cell growth after 24 hours, (b) spreading and alkaline phosphatase activity of cells at 3rd day on PEEK/rGO/cHAp at 20 µm, (c) 10 µm of PEEK cell spreading with tiny dead cells at 7th day on PEEK/rGO/cHAp (d) PEEK cell spreading more at 14th day, and (e-f) PEEK/rGO/cHAp with a dead cells at 14th day.

Molecules also bind to composite atoms and therefore are incorporated into the structure. Thus, the team can print an initial mixture of organic composite in a 3D structure. A 3D view of the binarised grain analysis results, after segmentation of hill detection, of PEEK/HAp is shown in Fig. 13. This figure shows the cell attachment of the PEEK/HAp composite. The DAPI (4′,6-diamidino-2- phenylindole) blue nuclear staining indicates the wide-scale presence of adherent cells throughout the composite substance. The strong scaffold green-channel autofluorescence competes with the cell tracker green signal, reducing the effectiveness of this assay. New bone formation is labelled with alizarin (red) and live/dead cell staining of S. mutans cultured calcein (green) in the image created using a robust Gaussian high-pass filter of 285 particles. The surface intercorrelation of the nanoparticles across the profile of binarised grains after segmentation of hill detection of PEEK/cHAp is shown in Fig. 13.
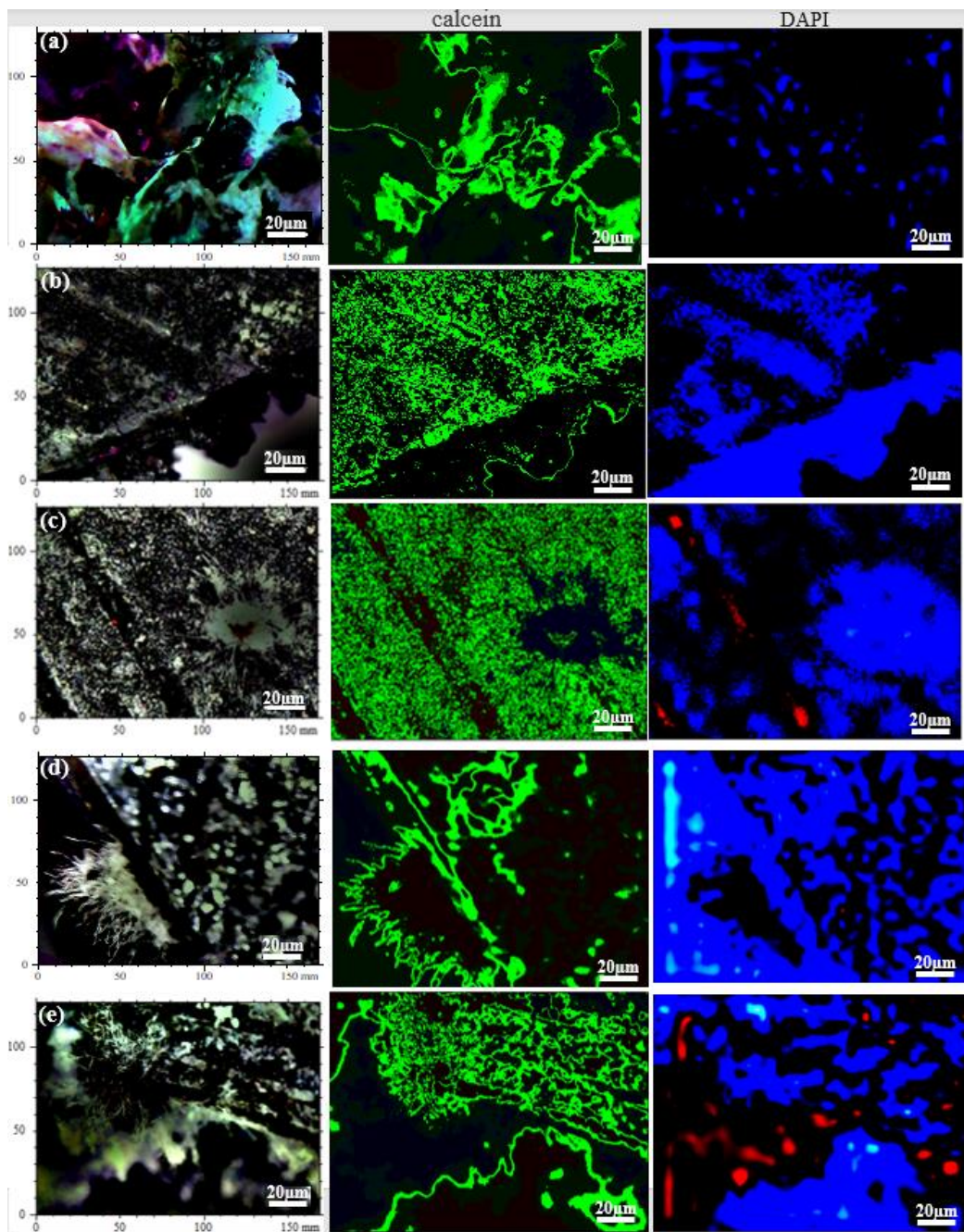
Fig. 13. (a) PEEK tested with DMEM, (b) PEEK/rGO/cHAp tested with DMEM, (c) PEEK tested with Nutrient Agar Solution and (d-e) PEEK/rGO/cHAp tested with Nutrient Agar Solution on different days.

Fig. 14 shows the binarised grain analysis results, after segmentation of hill detection, of PEEK/rGO/HAp and the surface intercorrelation of the nanoparticle analysis across the profile of the binarised grains, after the segmentation of hill detection, of PEEK/HAp. The frequency spectrum and tolerance limit test of the sample of reduced valley depth (Sck) and the luminance of the PEEK/HAp particles in grain/mm^2, are analysed. The resultant dominant spatial frequencies and maximum amplitudes at the 1st, 3rd and 7th days are 0.0144 mm^{-1} and 7000 GL^2, 0.013 mm^{-1} and 7987 GL^2, and 0.0124 mm^{-1} and 7822 GL^2, respectively. The complexity against nanoparticle scaling analysis is also shown in Fig. 10, as a scale-sensitive fractal analysis of the nanoparticle luminance of PEEK and fractal analysis of the brightness of the number of grains enclosing the box, to scale. The resultant texture and direction parameters of the converted luminance analysis of nanoparticles of PEEK/rGO/HAp in the ratios PEEK-69, cHAp-30, rGO-1 (wt%), PEEK-78, cHAp-20, rGO-2, and PEEK-87, cHAp-10, rGO-3, are anisotropy and first directional degree of 76.5% and 5.97 °C for the 1st day, 54.0% and 91.2 °C for the 3rd day, and 32.0% and 91.0 °C for the 7th day. Scatter plots of the square height parameters of nanoparticles with the ISO25178 standard, have second and third directional degrees of 37.8 and 171.0 °C for the 1st day, 97.0 and 179.0 °C for the 3rd day, and 136.0 and 63.0 °C for the 7th day. The crystalline structure is identified by XRD, using a Mountain 8.1 Premium digital surface diffractometer, and the results are shown in Fig. 14.
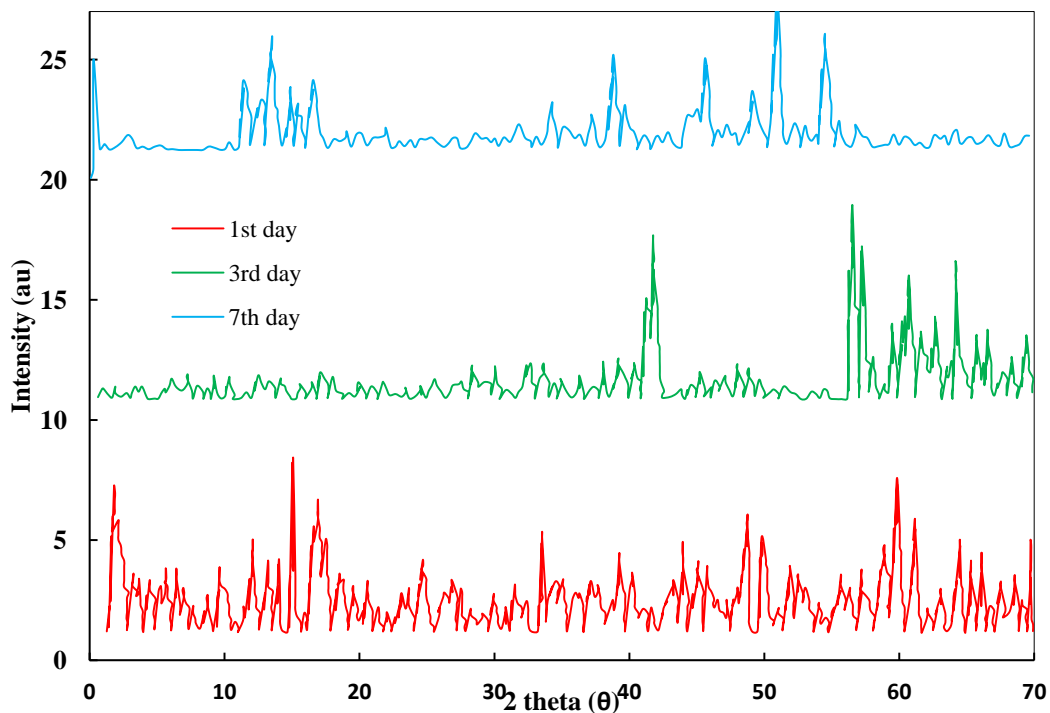
Fig. 14. Motifs analysis control chart of XRD pattern of the grain height of PEEK/cHAp fluorescence of counter-stained scaffold tissue engineering

7. Conclusion

PEEK biological activity is improved by adding cHAp and rGO particles for production by FDM. The mechanical properties and elastic moduli of PEEK/rGO/HAp composites with ratios PEEK-69, cHAp-30, rGO-1 (wt%), PEEK-78, cHAp-20, rGO-2, and PEEK-87, cHAp-10 and rGO-3 are evaluated. The PEEK-87, cHAp-10 and rGO-3 (wt%) composite exhibits the optimum stress of 25.32 GPa with a slight displacement of 9.29 mm, compared to the other ratios. PEEK/rGO/HAp composite induces apatite formation after immersion in DMEM simulated body fluid for 14 days. All the results confirm that, after uptake of cHAp and rGO, the biological activity of PEEK and osteogenesis are significantly improved.

It can be concluded that a numerical method of modular homogenisation of porous structures has been developed to effectively characterise the spatial distribution of the moduli and degree of anisotropy. Mapping the relationship between the geometric parameters and homogenisation coefficients has been undertaken to perform homogenisation control. The modulus spatial distribution response of solid material is shown in five lattice structures. The modulus of elasticity of trabecular bone for a porous structure with similar porosity is shown to be similar to two lattices, diamond and neovius. These structures mimic hip bone better than the others. The homogenisation difference between natural bone and porous structure is systematically compared to customised lattice pore structures for hip implants designed using 3D printing technology. The success of weight bearing porous hip implants depends on the lattice's ability to facilitate bone homogenised condensation and mimic the natural mechanical behaviours of femur bone.

Lastly, the present study can be considered a guide for a novel and high-resolution 3D printing of bone implant tissue scaffolds. It can be used to further compress moulds for bioactive PEEK/HAp composites. The modification of PEEK to produce essential derivatives with improved properties for tissue scaffold engineering is well investigated, showing that rGO and cHAp can be homogeneously dispersed in PEEK, and the compatibility between rGO/HAp and PEEK is improved, as required for biomedical engineering applications.

References

[1] M. Tafaoli-Masoule, M. Shakeri, S.A. Zahedi, H. Seitz, M. Vaezi, 3D printing of PEEK-based medical devices Transactions on Additive Manufacturing Meets Medicine 1 (1) (2019).

[2] A. Munaz, R.K. Vadivelu, J. St. John, M. Barton, N-T. Nguyen, Three-dimensional printing of biological matters, J. Sci. Adv. Mater Dev. 1 (1) (2016) 1-17.

[3] BI Oladapo, SA Zahedi, SO Ismail, FT Omigbodun, 3D printing of PEEK and its composite to increase biointerfaces as a biomedical material-A review, Colloids and surfaces. B, Biointerfaces 203, 111726-111726

[4] S. Li, SA. Zahedi, V. Silberschmidt, Numerical Simulation of Bone Cutting: Hybrid SPH-FE Approach, Numerical Methods and Advanced Simulation in Biomechanics and Biological Processes, (2017), Book chapter, 187-201

[5] S.K. Tiwari, S. Sahoo, N. Wang, A. Huczko, Graphene research and their outputs: Status and prospect, J. Sci. Adv. Mater. Dev. 5 (1) (2020) 10-29.

[6] OK Bowoto, BI Oladapo, SA Zahedi, FT Omigbodun, OP Emenuvwe, Analytical modelling of in situ layer-wise defect detection in 3D-printed parts: additive manufacturing, The International Journal of Advanced Manufacturing Technology (2020) 111 (7), 2311-2321

[7]   N. Abbasi, S. Hamlet, R.M. Love, N-T. Nguyen, Porous scaffolds for bone regeneration, J. Sci. Adv. Mater. Dev. 5 (1) (2020) 1-9.

[8]   BI Oladapo, SA Zahedi, S Chong, FT Omigbodun, IO Malachi, 3D printing of surface characterisation and finite element analysis improvement of PEEK-HAP-GO in bone implant, The International Journal of Advanced Manufacturing Technology 106 (3), (2020) 829-841

[9]   K.T.M. Tran, T.D. Nguyen, Lithography-based methods to manufacture biomaterials at small scales, J. Sci. Adv. Mater. Dev. 2 (1) (2017) 1-14.

[10]   M.H. Abdulkareema, A.H. Abdalsalam, A.J..Bohan, Influence of chitosan on the antibacterial activity of composite coating (PEEK /HAp) fabricated by electrophoretic deposition, Prog. Organic Coat. 130 (2019) 251-259.

[11]   S. Najeeb, M.S. Zafar, Z. Khurshid, F. Siddiqui, Applications of polyetheretherketone (PEEK) in oral implantology and prosthodontics, Journal of Prosthodontic Research, 60 (1) (2016) 12-19.

[12]   T.H.C.M.A. Song, Y.W. Lee, Characterisation of an inductively coupled nitrogen-argon plasma by Langmuir probe combined with optical emission spectroscopy, Phys. Plasmas 18 (2011) 023504.

[13]   J. Waser-Althaus, A. Salamon, M. Waser, C. Padeste, M. Kreutzer, U. Pieles, B. Müller, K. Peters, Differentiation of human mesenchymal stem cells on plasma-treated polyetheretherketone, J. Mater. Sci. Mater. Med. 25 (2014) 515-525.

[14]   B.I. Oladapo, S.A. Zahedi, A.O.M. Adeoye, 3D printing of bone scaffolds with hybrid biomaterials, Compos. Part B Eng. 158 (2019) 428-436.

[15]   B.I. Oladapo, S.A. Zahedi, F. Vahidnia, O.M. Ikumapayi, M.U. Farooq, Three-dimensional finite element analysis of a porcelain crowned tooth, Beni-Suef Univ. J. Basic Appl. Sci. 7 (4) (2019) 461-464.

[16]   B. Stawarczyk, M. Eichberger, J. Uhrenbacher, T. Wimmer, D. Edelhoff, P.R. Schmidlin, Three-unit reinforced poly ether ether ketone composite FDPs: Influence of fabrication method on load-bearing capacity and failure types, Dent. Mater. J. 34 (2015) 7-12.

[17]   D. Huang, X. Du, H. Liang, W. Hu, H. Hu, X. Cheng, Anterior corpectomy versus posterior laminoplasty for the treatment of multilevel cervical myelopathy: A meta-analysis, Int. J. Surg. 35 (2016) 21-27.

[18]   S. Wu, Z. Weng, X. Liu, K.W.K. Yeung, P.K. Chu, Functionalized TiO_2 based nanomaterials for biomedical applications, Adv. Funct. Mater. 24 (2014) 5464-5481.

[19]   C. Keul, A. Liebermann, P.R. Schmidlin, M. Roos, B. Sener, B. Stawarczyk, Influence of PEEK surface modification on surface properties and bond strength to veneering resin composites, Adhes. Dent. 16 (2014) 383-392.

[20]   O.P. Bodunde, O.M. Ikumapayi, E.T. Akinlabi, B. I. Oladapo, A.O.M. Adeoye, S.O. Fatoba, A futuristic insight into a "nano-doctor": A clinical review on medical diagnosis and devices using nanotechnology, Mater. Today Proc. (2020) 1-15.

[21]   B.I. Oladapo, S.A. Zahedi, S.C. Chaluvadi, S.S. Bollapalli, M. Ismail, Model design of a superconducting quantum interference device of magnetic field sensors for magnetocardiography, Biomed. Signal Proc. Cont. 46 (2019) 116-120.

[22] B.I. Oladapo, S.A. Zahedi, F.T.Omigbodun, E.A. Oshin, V.A. Adebiyi, O.B. Malachi, Microstructural evaluation of aluminium alloy A365 T6 in machining operation, J. Mater. Res. Technol. 8 (3) (2019) 3213-3222.

[23] S.A. Zahedi, M. Demiral, A. Roy, V.V. Silberschmidt, FE/SPH modelling of orthogonal micro-machining of fcc single crystal, Computational materials science (2013) 78, 104-109

[24] N.J. Usharani, A. Bhandarkar, S. Subramanian, S.S. Bhattacharya, Antiferromagnetism in a nanocrystalline high entropy oxide (Co,Cu,Mg,Ni,Zn)O: Magnetic constituents and surface anisotropy leading to lattice distortion, Acta Mater. 200 (2020) 526-536.

[25] Y. Zhu, X. Liu, K.W.K. Yeung, P.K. Chu, W. Shuilin, Biofunctionalization of carbon nanotubes/chitosan hybrids on Ti implants by atom layer deposited ZnO nanostructures, Appl. Surf. Sci. 400 (2017) 14-23.

[26] N. Ranjan, R. Singh, I.S. Ahuja, Biocompatible thermoplastic composite blended with HAp and CS for 3D Printing, Encycl. Renew. Sust. Mater. 4 (2020) 379-388.

[27] M. Alaña, A. Cutolo, B.V. Hooreweder, Understanding elastic anisotropy in diamond based lattice structures produced by laser powder bed fusion: Effect of manufacturing deviations, Mater. Des. 195 (2020) 108971.

[28] F.T. Omigbodun, B.I. Oladapo, O.K. Bowoto, F.P. Adeyekun, Experimental model design and simulation of air conditioning system for energy management, Int. Res..J. Eng. Technol. 6 (6) (2019) 811-816.

[29] O. Sproesser, P.R. Schmidlin, J. Uhrenbacher, M. Roos, W. Gernet, B. Stawarczyk, Effect of sulfuric acid etching of polyetheretherketone on the shear bond strength to resin cements, J. Adhes. Dent. 16 (2014) 465-472.

[30] M.K. Manglam, S. Kumari, M. Kar, Lattice strain caused magnetism and magnetocrystalline anisotropy in Zn modified barium hexaferrite, Phys. B Cond. Matter 588 (2020) 412200.

[31] F.T. Omigbodun, B.I. Oladapo, O.K. Bowoto, F.P. Adeyekun, Modelling detection of magnetic hysteresis properties with a microcontroller, Int. J. Eng. Trends Technol. 67 (6) (2019) 5-12.

[32] VA Balogun, BI Oladapo, Electrical energy demand modeling of 3D printing technology for sustainable manufacture, Int. J. Eng. 29 (7) (2019) 1-8.

[33] B.I. Oladapo, S.A. Zahedi, V.A. Balogun, S.O. Ismail, Y.A. Samad, Overview of additive manufacturing biopolymer composites, Encycl. Mater. Compos. (2021) 1-14.

[34] N.T. Evans, F.B. Torstrick, C.S.D. Lee, K.M. Dupont, D.L. Safranski, W.A. Chang, A.E. Macedo, A.S.P. Lin, J.M. Boothby, D.C. Whittingslow, R.A. Carson, R.E. Guldberg, K. Gall, High-strength, surface-porous polyether-ether-ketone for load-bearing orthopedic implants, Acta Biomater. 13 (2015) 159-167.

[35] D. Almasi, S. Izman, M. Assadian, M. Ghanbari, M.R. Abdul Kadir, Crystalline ha coating on PEEK via chemical deposition, Appl. Surf. Sci. 314 (2014) 1034-1040.

[36] Y.S. Al Jabbari, J. Fehrman, A.C. Barnes, A.M. Zapf, S. Zinelis, D.W. Berzins, Titanium nitride and nitrogen ion implanted coated dental materials, Coatings 2 (3) (2012) 160-178.

[37] D. Robinson, D. Alk, J. Sandbank, R. Farber, N. Halperin, Inflammatory reactions associated with a calcium sulfate bone substitute, *Ann Transplant*. 4 (3–4) (1999) 91-97.

[38] S. Hahnel, A. Wieser, R. Lang, M. Rosentritt, Biofilm formation on the surface of modern implant abutment materials, Clin. Oral Implants Res. 26 (11) (2014) 1297-1301.

[39] S.N.M. Jenkins, T.H. Oulton, R. Goodall, Anisotropy in the mechanical behavior of Ti6Al4V electron beam melted lattices, Mech. Res. Comm. 100 (2019) 103400.

[40] T. Lu, X. Liu, S. Qian, H. Cao, Y. Qiao, Y. Mei, P.K. Chu, C. Ding, Multilevel surface engineering of nanostructured TiO_2 on carbon-fiber-reinforced polyetheretherketone, Biomaterials 35 (2014) 5731-5740.

[41] N.T. Evans, F.B. Torstrick, C.S.D. Lee, K.M. Dupont, D.L. Safranski, W.A. Chang, A.E. Macedo, A.S.P. Lin, J.M. Boothby, D.C. Whittingslow, R.A. Carson, R.E. Guldberg, K. Gall, High-strength, surface-porous polyether-ether-ketone for load-bearing orthopedic implants, Acta Biomater. 13 (2015) 159-167.

[42] B.I. Oladapo, SA Zahedi, Improving bioactivity and strength of PEEK composite polymer for bone application Materials Chemistry and Physics (2021) 266, 124485

[43] B. I. Oladapo, S. A. Zahedi, S. O. Ismail, F. T. Omigbodun, O.K. Bowoto, M. A. Olawumi, M. A. Muhammad, 3D printing of PEEK–cHAp scaffold for medical bone implant, Bio-Design and Manufacturing (2021) 4 (1), 44-59